# High photocatalytic performance of ruthenium complexes sensitizing g-C₃N₄/TiO₂ hybrid in visible light irradiation

Guodong Jiang[a,*], Ke Geng[a], Ye Wu[b,**], Yinhui Han[c], Xiaodong Shen[a]

[a] College of Materials Science and Engineering, Nanjing Technology University, Nanjing, 210009, China
[b] School of Energy and Power Engineering, Nanjing University of Science and Technology, Nanjing, 210094, China
[c] North China Electric Power University, Baoding, 071003, China

ARTICLE INFO

ABSTRACT

Ruthenium (II) was firstly coordinated with 4,4′-dicarboxy-2,2′-bipyridine for 4,4′-dicarboxy-2,2′-bipyridine ruthenium and then bonded with g-C₃N₄ (designated as RuC@g-C₃N₄), and were finally loaded in TiO₂ (designated as RuC@g-C₃N₄/TiO₂) by the solvothermal method. The obtained ruthenium complexes sensitizing g-C₃N₄/TiO₂ hybrid exhibited high photocatalytic performance under the visible light irradiation. The morphologis of photocatalysts were characterized by field emission scanning electron microscopy (FE-SEM), high-resolution transmission electron microscopy (HRTEM) with element mapping and Brunauer-Emmett-Teller (BET). The compositional structure and chemical composition were analyzed by X-ray diffraction (XRD), X-ray photoelectron spectroscopy (XPS), and Fourier transform infrared spectra (FTIR). Photoluminescence (PL) spectra indicated the addition of the ruthenium complexes enhanced the photo-generated electron-hole separation and transport, and the photocatalytic activity was evaluated by degradation of Methyl Blue (MB) under visible light irradiation. The results suggest that the minor amounts of ruthenium complexes sensitizing can usefully improve the photocatalytic performance, and the optimal theory mass ratio of TiO₂ to RuC@g-C₃N₄ of 12:1 presents the best catalytic performance, and it is nearly 1.9 times as high as the conventional reported optimal g-C₃N₄/TiO₂ hybrid with the same mass ratio of TiO₂/g-C₃N₄ of 12:1 under visible light irradiation. At the end of article, a possible photocatalytic mechanism was discussed based on the experimental results.

## 1. Introduction

A wide range of water pollution has become a major global problem to be urgently solved, wherein the organic water pollution, which is mainly attributed to domestic sewage, agricultural and industrial waste water, has especially aroused great attention. Treatment methods often include oxidation processing [1], membrane filtration [2], adsorption [3], chemical immobilization [4], biological degradation [5] and so on. Some of these treatment methods would have placed a heavy burden on many developing countries due to high treatment cost, thus the high efficient treatment and low treatment cost of organic waste water is still a big challenge. Recently, visible photocatalytic degradation is considered to be a potentially significant strategy for removing trace contamination without secondary pollution. This visible photocatalyst powder only needs to directly be dispersed in wastewater and can degrade continually organic contaminants through the solar, which would have tremendous application value to many developing countries.

Since Fujishima and Honda [6] reported the photocatalytic splitting water on the surface of TiO₂ under UV light irradiation in 1970s, the degradation of organic pollutant had been gradually investigated. Unfortunately, TiO₂, a low-cost, non-toxic semiconductor photocatalyst, stable over the long term, was initially investigated in ultraviolet (UV) light in about 5% of natural solar light. Therefore, how to improve the visible photocatalytic degradation efficiency of TiO₂ has always been the primary challenge. In order to extend the adsorption edge of TiO₂ and suppress the recombination of $e^-$-$h^+$ pairs, many attempts have been presented such as introducing minor amounts of other elements into the lattice and controlling structure (e.g. nonmetals B, C, N, S and P, or transition metals V, Fe, Cr, Nb, and Mn [7–16], etc.), or compositing with other semiconductors. Since graphitic carbon nitride (g-C₃N₄)'s intrinsic structure includes tri-s-triazine units, it has recently attracted significant attention as a metal-free semiconductor for visible-light absorbing ability up to 450 nm. However, the high recombination rate of the photogenerated electrons and holes pairs ($e^-$/$h^+$) in g-C₃N₄ depresses its photocatalytic efficiency. Thus, g-C₃N₄ coupling with various semiconductors (such as TiO₂, MoS₂, CdS and ZnS, etc.) has

been one of the more effective methods through the heterojunction in semiconductor composite material to improve the separation efficiency of the photogenerated electrons and holes ($e^-$/$h^+$) [17–20]. Among these semiconductors, there have been several reports about the photocatalytic performance of g-$C_3N_4$/$TiO_2$ composites. Irvine et al. [21] prepared the g-$C_3N_4$/$TiO_2$ nanotube hybrids by simple solid sublimation and transition method using urea as precursor, which exhibited better photoelectron chemical performance in sewage treatment. Wang et al. [22] synthesized g-$C_3N_4$/mesoporous $TiO_2$ hybrids by growth of g-$C_3N_4$ on mesoporous $TiO_2$ spheres, which showed much higher photocatalytic performance than that of pure $TiO_2$ and g-$C_3N_4$ under both UV light and visible light irradiation. In our previous studies [23,24], the nanosheet $TiO_2$/g-$C_3N_4$ and further nanosheet $TiO_2$/phosphorus-doped g-$C_3N_4$ heterogeneous photocatalysts perfomed an excellent performance of visible photocatalytic degradation. Besides fabricating the heterojunction between $TiO_2$ and g-$C_3N_4$, increase of photon absorbing efficiency also performs key factor for improving photocatalytic performance. Photosensitizer is a molecule that absorbs photon and transfers the energy to another molecule and promotes their chemical reaction, but itself does not participate in the chemical reaction. So, it is significant to introduce the photosensitizer to $TiO_2$/g-$C_3N_4$ heterogeneous photocatalyst for increasing the quantity of photons absorption. Since Meyera et al. [25] reported that the [Ru(bpy)$_3$]$^{2+}$ had the ability to convert light energy into chemical energy in 1975, ruthenium complexes became one of the most widely studied photosensitizer due to its stable chemical properties, strong electron transporting ability, and relatively long excited state [26,27]. The valence electron configuration of ruthenium atoms is $4d^7 5s^1$, which is easily to form the stable low spin coordination compounds between ruthenium atoms and pyridine ligands by $d^2 sp^3$ hybrid mode. Ruthenium (II) acts as the co-ordination center and binds the pyridine ligand to form six coordinate non-planar structure, which causes the quantum efficiency of the photocatalyst in various photocatalytic reactions [28,29]. Nazeeruddin et al. [30] conducted a study on the use of 2,2'-bipyridyl-4,4'-dicarboxylate ruthenium as a photosensitizer for the application of solar cells. Maeda et al. [31] used $C_3N_4$ coupled with ruthenium complexes as a catalyst for $CO_2$ reduction into HCOOH under visible light. Kowalska et al. [32] reported ruthenium complexes sensitized $TiO_2$ on visible light exhibited the highest level of photocatalytic performance. However, to the best knowledge of the authors, little literature for the ruthenium complexes sensitizing g-$C_3N_4$/$TiO_2$ hybrid are reported to further improve the photocatalytic activity of the photocatalyst. In the paper, a novel ruthenium complexes-based composite was studied in this paper. The ruthenium complexes as an photosensitizer was fixed on the g-$C_3N_4$ using the amino groups of g-$C_3N_4$, and then the synthetic ruthenium complexes@g-$C_3N_4$ was loaded on the surface of $TiO_2$ by solvothermal synthesis. The morphology and structural properties of the resulting ruthenium complexes@g-$C_3N_4$/$TiO_2$ hybrids were analyzed by XRD, BET and SEM. Further the chemical structures were characterized by FITR and XPS. PL was performed to determine the recombination efficiency of the photocatalyst. The photocatalytic activity was evaluated by degradation of Methyl Blue under visible light irradiation.

## 2. Experimental

### 2.1. Preparation of photocatalyst

#### 2.1.1. Preparation of 4,4'-dicarboxy-2,2'-bipyridine

4,4'-Dimethyl-2,2'-bipyridine (2.098 g, 11.39 mmol) was mixed in 98 wt.% of $H_2SO_4$ (60 mL) with stirring at room temperature for 20 min, then $K_2Cr_2O_7$ (10.432 g, 35.46 mmol) was added gradually into the resulting solution with vigorous stirring at 0 °C for 2 h. After that, the mixture solution was heated for 10 h at 70 °C with stirring and the resulting deep green solution was poured into a beaker containing 500 mL ice water for white precipitate. After the obtained white precipitate was
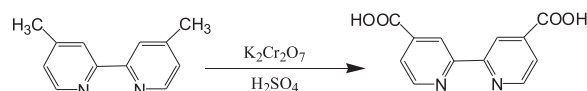


**Fig. 1.** Preparation of 4,4'-dicarboxy-2,2'-bipyridine.

filtered and washed with water, it was dissolved in NaOH solution, and then the insoluble matter was filtered out. Finally, the excessive hydrochloric acid was dropped in the dissolved solution for producing precipitate of 4,4'-dicarboxy-2,2'-bipyridine, then filtered and washed with water by twice and the yield of 93.8 wt.% was obtained, as shown in Fig. 1. The important structural feature of 4,4'-dicarboxy-2,2'-bipyridine may provide two bidentate sites for coordination.

#### 2.1.2. Preparation of [Ru(4,4'-dicarboxy-2,2'-bipyridine)$_3$]Cl$_2$

0.353 g of RuCl$_3$(3H$_2$O) and 0.981 g of 4,4'-dicarboxy-2,2'-bipyridine were placed in a hydrothermal reactor, where 7 mL of HCl and 14 mL of water were added. The mixture solution was heated at 200 °C for 5 h and cooled gradually to room temperature. The dark red precipitate was filtered off from the obtained brown suspension solution and washed with a small amount of water. The dark red powder was achieved through several recrystallizations from water, which resulted in a final yield of 85.1 wt.% as shown in Fig. 2. The achieved [Ru(4,4'-dicarboxy-2,2'-bipyridine)$_3$]Cl$_2$ (designated as RuC) was proved by comparison of the crystal powder diffraction of product powder and the simulated curve based on CCDC crystal library [33] as shown in Fig. S3 of Supplementary Material.

#### 2.1.3. Preparation of g-$C_3N_4$

The carbon nitride (g-$C_3N_4$) was synthesized by heating melamine powder as precursor at 520 °C for 3 h, and further heat exfoliation at 550 °C for 2 h.

#### 2.1.4. Preparation of [Ru(4,4'-dicarboxy-2,2'-bipyridine)$_3$]Cl$_2$@g-$C_3N_4$

A designated mass [Ru(4,4'-dicarboxy-2,2'-bipyridine)$_3$]Cl$_2$ was treated in refluxing SOCl$_2$ (30 mL) under N$_2$ for 24 h to generate [Ru(4,4'-diformyl chloride-2,2'-bipyridine)$_3$]Cl$_2$, then 50 mL methylbenzene was added in the obtained dark red solution and excess SOCl$_2$ was completely removed by distillation under mild heating conditions. 3 g g-$C_3N_4$ was dispersed into the obtained [Ru(4,4'-diformyl chloride-2,2'-bipyridine)$_3$]Cl$_2$ in refluxing methylbenzene solvent for 12 h. The formyl chloride would react with the amino groups of g-$C_3N_4$ [34]. After the reaction, removed the methylbenzene by distillation, and then the product was washed by three times with 40 °C water and ethanol respectively. Finally, [Ru(4,4'-dicarboxy-2,2'-bipyridine)$_3$]Cl$_2$@g-$C_3N_4$ (designated as RuC@g-$C_3N_4$) was successfully obtained as shown in Fig. 3 [35].

#### 2.1.5. Preparation of [Ru(4,4'-dicarboxy-2,2'-bipyridine)$_3$]Cl$_2$@g-$C_3N_4$/$TiO_2$ hybrid

[Ru(4,4'-dicarboxy-2,2'-bipyridine)$_3$]Cl$_2$@g-$C_3N_4$/$TiO_2$ (designated as RuC@g-$C_3N_4$/$TiO_2$) hybrid was prepared by the solvothermal method. The mixture suspension solution including a designated mass RuC@g-$C_3N_4$, 6.8 g of tetrabutyl titanate (TBT) and 50 mL of isopropanol was treated by ultrasonic dispersion for 30 min, and then 1.5 mL of hydrofluoric acid (40 wt.%) was added into the resulting suspension solution with magnetic stirring for 10 min. After that, the mixture suspension solution was sealed into a Teflon-lined autoclave at 180 °C for 12 hours h. The powder RuC@g-$C_3N_4$/$TiO_2$ hybrids were obtained through high-speed centrifugation and drying at 80 °C for 5 h. According to the theory mass ratio of $TiO_2$ to RuC@g-$C_3N_4$ of 14:1, 12:1, 6:1 and 4:1, and they were denoted as G14-1, G12-1, G6-1 and G4-1, respecitvely. In order to evaluate the effect of ruthenium complexes sensitizing on photocatalysts, the $TiO_2$ and $TiO_2$/g-$C_3N_4$ hybrid without RuC were fabricated by the same solvothermal method, and the $TiO_2$/g-$C_3N_4$ hybrid with the theory mass ratio of $TiO_2$ to g-$C_3N_4$ of
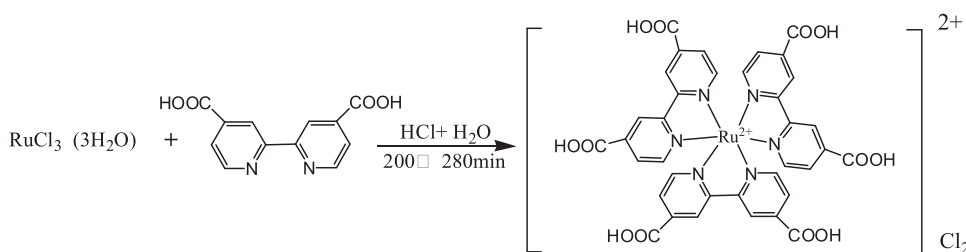
12:1 was designated as H12-1. According to the content of RuC in G12-1, [Ru(4,4′-dicarboxy-2,2′-bipyridine)₃]Cl₂@TiO₂ (designated as RuC/TiO₂) with about 0.45 wt.% of RuC was prepared by the same solvothermal method.

## 2.2. Characterizations

The crystal phases of the samples were measured by X-ray Diffraction (XRD) with Cu $K\alpha$ ($\lambda$ = 0.15418 nm) radiation on a SmartLab diffractometer (Japan), and the diffractograms were recorded with a $2\theta$ range of 10–80° with a normal scan speed of 10°/min. The Fourier transform infrared spectra (FTIR) of the powder samples were acquired on the Nicolet iN10 FT-IR spectrometer with the powder samples mixed in KBr at the range of 400–4000 cm$^{-1}$. UV–vis diffused reflectance spectra (UV–vis DRS) were conducted on UV–vis spectrometer (UV-3600, Shimazu, Japan) with BaSO₄ used as the reference standards. Photoluminescence (PL) spectra were recorded using a 320 nm excitation light source at 25 °C (Horiba Jobin Yvon FL3-TCSPC). The morphologies of powder samples were observed on a field emission scanning electron microscope (FESEM, ULTRA 55, Zeiss, Germany) and high-resolution transmission electron microscopy (HRTEM, Tecnai G2 F30, FEI, USA) with element mapping. The specific surfaces of photocatalysts are determined by multi-point Brunauer, Emmett and Teller (BET) method using the nitrogen adsorption/desorption (Micromeritics ASAP 2020, USA) isotherms. X-ray photoelectron spectroscopy (XPS) was measured on a PHI 5000 Versaprobe spectrometer with Al $K\alpha$ radiation as the excitation source.

## 2.3. Photodegradation test

The photocatalytic activities of as-obtained samples were evaluated by the decomposition of Methylene Blue (MB) under visible light irradiation. A quantity of photocatalysts were poured in aqueous solution of MB, and then the samples were irradiated by Xenon long-arc lamp (Special lighting Electric Appliance Factory, Shanghai) with 500 W, whose spectrum is shown in Fig. S2 of Supplementary material. The UV light portion of Xenon lamp was filtered out by ultraviolet cut-off filters (> 400 nm). The average distance between the light source and the liquid in the reactor is about 3 cm, and the average visible intensity was measured to be 205 mW/cm$^2$ by an optical power metre. The concentration of MB in the solution was measured by its absorbance at 620 nm with a UV–vis spectrophotometer (UV-3200, Mapada, China) every 15 min. The detail test was descripted in Supplementary Material.

## 3. Results and discussion

### 3.1. XRD analysis

The full-range XRD patterns of different photocatalysts are displayed in Fig. 4. In Fig. 4a, a typical (100) weak diffraction peak around 12.9° corresponding to a distance of 0.676 nm is attributed to the in-plane repeated tri-s-triazine units of g-C₃N₄. The (002) diffraction band is independently shown in Fig. 4b. In Fig. 4b, the peak around 27.4° corresponding to interlayer distance of about 0.325 nm is attributed to stacking of the conjugated nitrogen-containing aromatic ring of bulk g-C₃N₄ [36], while the peak appearing around 27.2° may be due to the g-C₃N₄ covered TiO₂ [37]. As seen on G4-1, G6-1, G12-1 and G14-1, the peak intensities around 27.2° becomes weak with the content of g-C₃N₄ decreasing until G12-1 completely disappears. In addition, the diffraction angles at $2\theta$ = 25.3°, 37.8°, 48.0°, 53.9°, 55.1°, 62.7° and 70.3° correspond to the (101), (004), (200), (105), (211), (204) and (116) crystal planes of anatase TiO₂ (JCPDS 21-1272) [38], which suggests that the prepared RuC@g-C₃N₄/TiO₂ hybrids still retain anatase TiO₂ grain structure.

### 3.2. FT-IR analysis

FTIR spectra of RuC, g-C₃N₄, RuC@g-C₃N₄, and different RuC@g-C₃N₄/TiO₂ hybrids [G4-1, G6-1, G12-1, and G14-1] are presented in Fig. 5. RuC has one strong absorption at 1721 cm$^{-1}$ for carboxyl group which can be used to react with SOCl₂, and the broad peaks at around 3420 cm$^{-1}$ and 2936 cm$^{-1}$ are attributed to the −OH and CH stretching vibration mode, respectively. g-C₃N₄ and RuC@g-C₃N₄ have the absorptions at 811 cm$^{-1}$, 1635 cm$^{-1}$, and 1572 cm$^{-1}$ corresponding to the breathing mode of triazine units [39,40], C═N stretching vibration mode [41], and C−N heterocycle stretching of g-C₃N₄ [42], respectively. However these above peaks disappear due to the low content of g-C₃N₄ in G4-1, G6-1, G12-1 and G14-1. g-C₃N₄ and



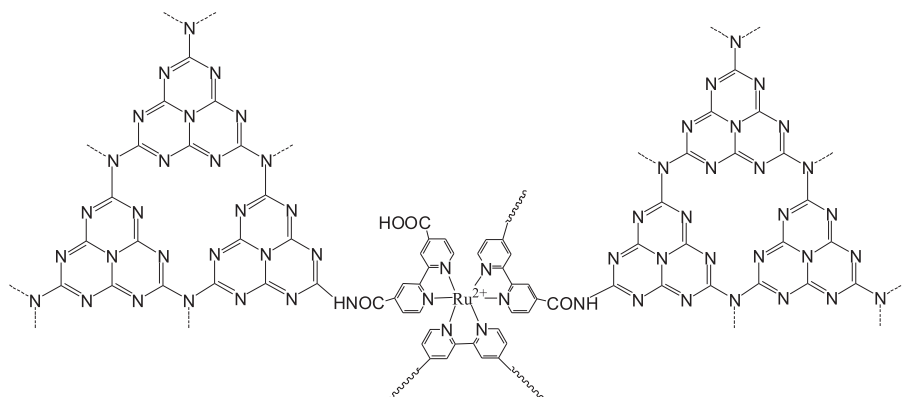**Fig. 3.** Schematic of [Ru(4,4′-dicarboxy-2,2′-bipyridine)₃]Cl₂@g-C₃N₄.
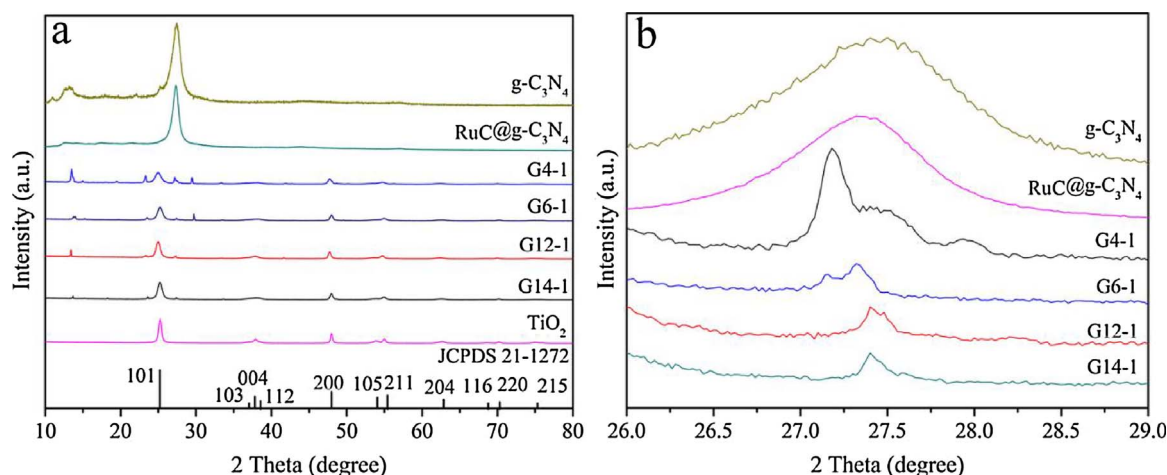
**Fig. 4.** XRD patterns of g-C$_3$N$_4$, RuC@g-C$_3$N$_4$, TiO$_2$ and different RuC@g-C$_3$N$_4$/TiO$_2$ hybrids [G4-1, G6-1, G 12-1 and G14-1].
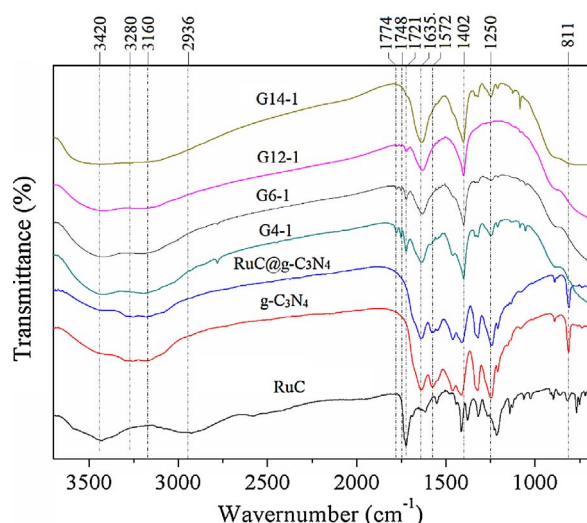


**Fig. 5.** FTIR spectra of RuC, g-C$_3$N$_4$, RuC@g-C$_3$N$_4$, and RuC@g-C$_3$N$_4$/TiO$_2$ hybrids [G4-1, G6-1, G12-1, and G14-1].

RuC@g-C$_3$N$_4$ have almost no absorption in 1700–1800 cm$^{-1}$ region, which are assigned to the C═O stretching vibration mode due to low content of C═O [43]. However there are three bands at 1721 cm$^{-1}$, 1748 cm$^{-1}$ and 1774 cm$^{-1}$ corresponding to the carbonyl on the different ortho-positions of nitrogen of g-C$_3$N$_4$ for G4-1, G6-1, G12-1 and G14-1, and the absorption intensity of the C═O bond decreases with the decrease of RuC@g-C$_3$N$_4$ content due to of tri-s-triazine units under TiO$_2$ as catalyzer, which has been fully illustrated for the formation mechanism of carbonylation in our previous literature [23]. In addition, the peak around 1402 cm$^{-1}$ is attributed to the bending vibration of O─H bonding with carbon from carboxyl and the broad peaks at around 3280 cm$^{-1}$ and 3160 cm$^{-1}$ are attributed to the stretching modes of terminal ─NH and ─NH$_2$ groups of g-C$_3$N$_4$, respectively [44,45].

### 3.3. XPS analysis

XPS measurement can be carried out to accurately analyze the surface chemical composition and different status of the photocatalyst. The full-range XPS spectrum indicates the peaks of N1s, O1s, C1s, Cl2p, Cl2s and Ru3p on the surface of the g-C$_3$N$_4$, RuC and sample RuC@g-C$_3$N$_4$ as shown in Fig. S4 of Supplementary Material, respectively. The O1s peak is attributed to the oxidation of g-C$_3$N$_4$ in high-temperature heating air, and the O1s peak of RuC becomes stronger due to high ratio of carboxyl. In the C1s region of g-C$_3$N$_4$, the mainly carbon species can be

deconvoluted into four components, the binding energy values at 284.7 eV can be assigned exclusively to C─C due to the formation of amorphous sp2-hybridized carbon during preparation of g-C$_3$N$_4$ [46], the peaks at 286.1 eV and 288.2 eV are identified as the sp2-hybridized carbon atom with C─NH─C between two tri-s-triazine units and nitrogen-center in tri-s-triazine units, respectively, more C1s peaks can be found at 288.9 eV and 293.3 eV corresponding respectively to carboxyl and the carbon attached to uncondensed terminal NH$_2$ species in nitrogen-containing aromatic ring. For the RuC, the peaks at 284.7 eV and 288.2 eV can be attributed to C─C and the carbon atom bonding with nitrogen atom in pyridine ring, the peak at 288.6 eV refers to carboxyl with pyridine ring which is different with nitrogen-containing aromatic ring, and another weak peak detected at 291.5 eV can be assigned exclusively to pi → pi*, notably the peak at 285.4 eV can be ascribed to Ru 3d$_{3/2}$. In Fig. 6b, the main N1s peak of g-C$_3$N$_4$ can be separated into three obvious peaks at 398.7 eV, 400.1 eV, and 401.3 eV indicating three types of N bonding, the signal peak at 398.7 eV can be related to the sp$^2$ hybridized nitrogen (C═N─C) involved in triazine rings, the peak at 400.1 eV can be identified as the nitrogen-center atom in tri-s-triazine units [47], and the peak at 401.3 eV can be assigned to amino group (N─H) [48], another independent broad peak at 403.1 eV can be attributed to the pi → pi*, a single peak at 399.8 eV of RuC can be related to the nitrogen in pyridine ring. In the O1s spectrum of Fig. 5c, for the, the peaks at 532.1 eV and 533.5 eV of g-C$_3$N$_4$ are ascribed to ─OH and O═C groups, however the binding energies of these groups deviate to 531.3 eV and 532.9 eV, respectively. In Fig. 5d, the Ru3d$_{5/2}$ spectrum can reveal the valence state of ruthenium in RuC, the peak at 280.4 eV is ascribed to Ru$^{2+}$, this is probably due to the formation of coordination bonds between ruthenium and ligands. In this process, the ligands provide lone pair electrons to ruthenium, which gently leads to the electron density of ruthenium increased, thus gradually reduced the attraction for the extra nuclear electron and the binding energies of ruthenium were reduced to 280.4 eV compared to normal binding energy of Ru$^{2+}$ (281.3 eV) [49]. The peak at 280.8 eV is ascribed to Ru$^{\delta+}$, the binding energy is slightly higher than the Ru$^{2+}$ (280.1 eV) because the ruthenium complexes molecule is likely to remove one or two ligands, which increase the binding energy of Ru$^{\delta+}$ [50]. In addition, the different binding energy curves of RuC@g-C$_3$N$_4$ are very similar to g-C$_3$N$_4$ due to low content of RuC as shown in Fig. 6 and Fig. S4 of Supplementary Material.

The atomic content of photocatalyst would also be discussed using XPS as shown Table 1. In Table 1, the atomic contents of tested g-C$_3$N$_4$ and RuC are closed to stoichiometric ratio. According to 0.06 atomic% of Ru in tested RuC@g-C$_3$N$_4$, the mass content of RuC could be infer to about 5.7 wt.% in RuC@g-C$_3$N$_4$, and further, the mass contents of RuC and Ru could be calculated as about 0.44 wt.% and 0.054 wt.% of G12-1, respectively.
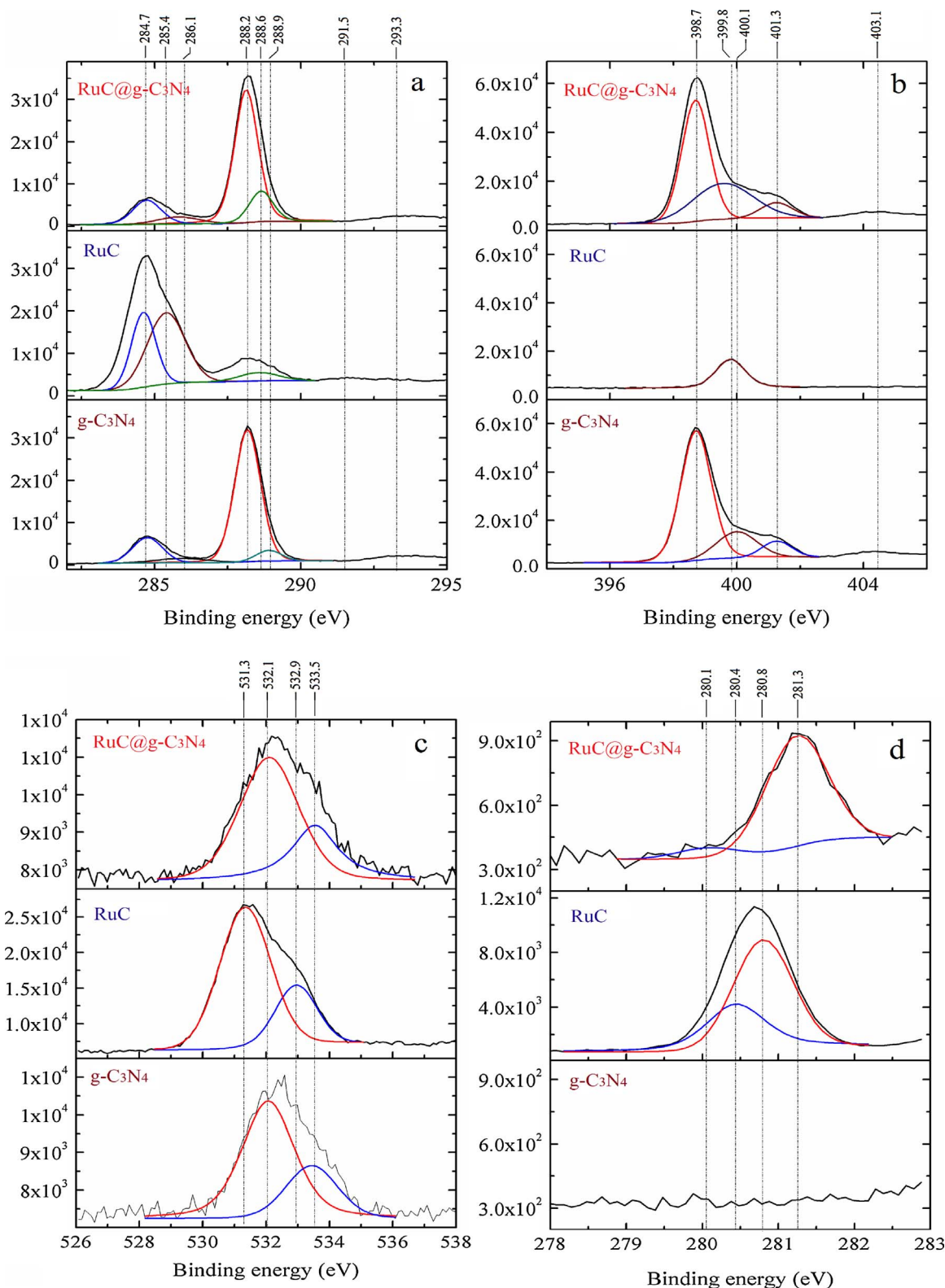
**Fig. 6.** XPS spectra of g-C$_3$N$_4$, RuC and RuC@g-C$_3$N$_4$ including C1s (a), N1s (b), O1s (c), Ru3d$_{5/2}$ (d).

### 3.4. BET analysis

Nitrogen Adsorption-Desorption (NAD) isotherms of RuC@g-C$_3$N$_4$(a) and the RuC@g-C$_3$N$_4$/TiO$_2$ hybrid (G12-1) (b) at 77 K are plotted in Fig. 7. The NAD isotherm of RuC@g-C$_3$N$_4$ (a) is keeping with g-C$_3$N$_4$'s due to low content of RuC as shown in Table. 1 and Fig. S5 of Supplementary Material. It is a classical adsorption-desorption isotherm

for aggregates (loose assemblages) of plate like particles forming slit-like pores, reveals the structure of nanosheet g-C$_3$N$_4$ stacking together. For G12-1 as shown in Fig. 7b, it is a type IV of adsorption-desorption isotherm for mesoporous solid, and the total pore volume and average pore size of G12-1 are less than that of RuC@g-C$_3$N$_4$ in contrary to the specific surface as shown in Table 2.

**Table 1**
The atomic contents of tested samples.

| Atomic% | g-$C_3N_4$ | | RuC | | RuC@g-$C_3N_4$ |
|---|---|---|---|---|---|
| | Tested | Stoichiometry | Tested | Stoichiometry | Tested |
| C1S | 44.46 | 42.86 | 69.79 | 65.45 | 44.58 |
| N1S | 51.63 | 57.14 | 9.6 | 10.91 | 51.33 |
| O1S | 3.9 | | 21.18 | 21.82 | 4.03 |
| Ru3d5/2 | | | 1.25 | 1.82 | 0.06 |

**Table 2**
Physical constant of samples detected by nitrogen adsorption-desorption.

| | g-$C_3N_4$ | RuC@g-$C_3N_4$ | G12-1 |
|---|---|---|---|
| Average pore size (nm) | 24.9 | 24.6 | 8.4 |
| Total pore volume ($cm^3$/g) | 0.185 | 0.179 | 0.131 |
| Specific surface area ($m^2$/g) | 29.1 | 29.1 | 62.3 |

### 3.5. FESEM and HRTEM analysis

Morphological evaluations of and g-$C_3N_4$ (a) (b), RuC@g-$C_3N_4$ (c) (d), and RuC@g-$C_3N_4$/$TiO_2$ hybrid (G12-1) (e) (f) were performed by FESEM analysis. The shapes of g-$C_3N_4$ (a) (b), RuC@g-$C_3N_4$ (c) (d), and G12-1 (e) (f) are irregular powder and wide diameter distribution as shown in Fig. 8a, c and e. The magnified image of g-$C_3N_4$ (b) displays the porous structure with about 50 nm nanoparticles stacking as shown in Fig. 8b. After ruthenium complexes is immobilized in the g-$C_3N_4$, the magnified image of RuC@g-$C_3N_4$ (d) presents a sponge-like surface as shown in Fig. 8d. In Fig. 8e and f, the structure of G12-1 powder exhibits layers stacking, and it can be clearly seen that $TiO_2$ crystal growth on the surface of G12-1 powder due to the tetrabutyl titanate soaking into the layer of g-$C_3N_4$ and generating square flake-like $TiO_2$ crystal with the side length 50–60 nm and he thickness of 10–15 nm in the hydrothermal synthesis process.

As shown in Fig. 9a and b, the powder RuC@g-$C_3N_4$ is composited of the pore about 50 nm and the multiple-layered frame structure. For G12-1 as shown in Fig. 9, the square flake-like $TiO_2$ crystals stack together and there is g-$C_3N_4$ in the space between $TiO_2$ crystals with the active (101) crystal plane distance of 0.35 nm, which suggests the interface of hetero-structure between g-$C_3N_4$ and $TiO_2$. Further, the element mapping could demonstrate the existence of C, N, O, Ti and minor Ru elements as shown in Fig. 10. The equidistribution of C, N, O and Ru elements in the profile of RuC@g-$C_3N_4$ powder is shown in Fig. 10a. However, the source of C and N elements is mainly attributed to g-$C_3N_4$ due to only 0.44 wt.% of RuC in G12-1, which suggests the existence of hetero-structure between g-$C_3N_4$ and $TiO_2$ as shown in Fig. 10b.

### 3.6. PL analysis

For understanding the trapping, immigration and transfer property of electron-hole pairs, the PL emission intensity can be employed to determine the separation efficiency of photogenerated electron-hole pairs. It is well known that the intensity of the PL spectra depend on the recombination of excited electrons and holes. Generally, a low PL intensity indicates a decrease in the recombination rate of photogenerated electron-hole pairs. Fig. 11 displays the PL emission spectra of different g-$C_3N_4$/$TiO_2$ hybrid (H12-1), RuC@g-$C_3N_4$/$TiO_2$ hybrids, RuC@g-$C_3N_4$, g-$C_3N_4$ and $TiO_2$ at room temperature. The broad PL band of g-$C_3N_4$ is from 400 nm to 550 nm, which mainly results from the n-π* electronic transitions involving lone pairs of nitrogen-containing aromatic ring, Further, the g-$C_3N_4$ immobilized by minor ruthenium complexes can substantially reduce the PL intensity, which suggests that the addition of ruthenium complexes can increase the separation efficiency of photogenerated electron-hole pairs. The $TiO_2$ exhibits a weak emission in the wavelength range of 360–450 nm, which does not mean lower carrier recombination [51], but also low absorption to excitation light (320 nm). For g-$C_3N_4$/$TiO_2$ hybrid (H12-1), although the content of $TiO_2$ is well above g-$C_3N_4$, the broad band about 440 nm shows the intensity markedly decreases because the tight heterojunction of g-$C_3N_4$/$TiO_2$ hybrid efficiently suppresses the recombination of photogenerated electron-hole pairs, which performs excellent photocatalytic performance under visible light irradiation. For the different RuC@g-$C_3N_4$/$TiO_2$ hybrids (G14-1, G12-1, G6-1 and G4-1) in Fig. 9b, there are two emission peaks of G4-1 around 396 nm and 430 nm corresponding to superposition of $TiO_2$ and g-$C_3N_4$ emission peaks, respectively. Wherein the obvious blue shift from intrinsic peak at 465 nm of g-$C_3N_4$ to 430 nm for G4-1 is due to the exfoliated RuC@g-$C_3N_4$ into more thin nanosheet g-$C_3N_4$ during the preparation of RuC@g-$C_3N_4$/$TiO_2$ hybrids in solvothermal synthesis causes the well-known quantum confinement effect [52], and the intensity markedly would decrease with the content of g-$C_3N_4$ decreases, as a result, the peak of H12-1, G14-1, G12-1 and G6-1 corresponding to g-$C_3N_4$ can disappear because of low content of g-$C_3N_4$. In addition, It is interesting that the peak emitted by $TiO_2$ displays a red shift from intrinsic peak at 388 nm to 396 nm of RuC@g-$C_3N_4$/$TiO_2$ hybrids due to the lower π* orbital of the 4,4′-dicarboxy-2,2′-bipyridine ligand [53]. Compared with the H12-1, the lower intensity of RuC@g-$C_3N_4$/$TiO_2$ hybrids except G4-1 suggest to the ruthenium complexes can greatly promote the effective separation of photogenerated electron-hole pairs, and the lowest intensity of G12-1 performs highest photocatalytic performance.

### 3.7. UV–vis DRS analysis

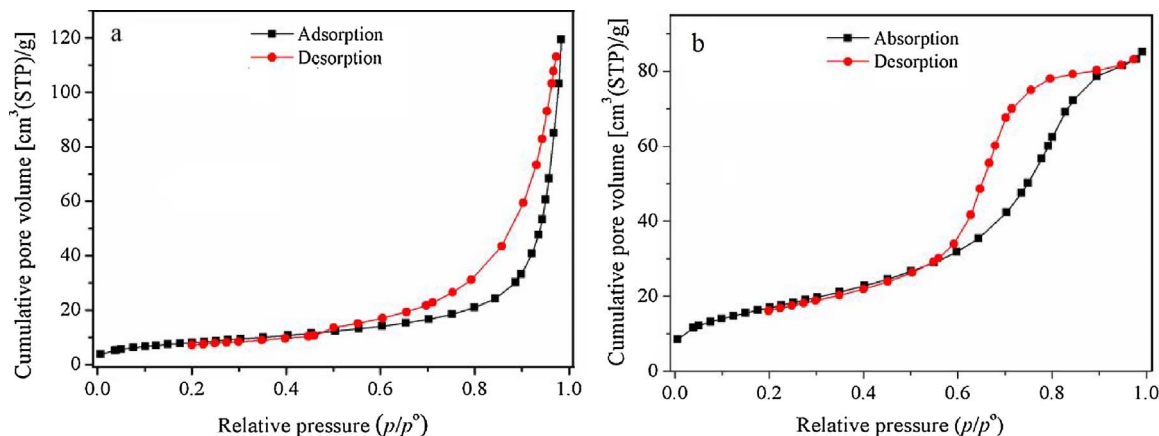The UV–vis DRS is used to investigate optical absorption behavior.



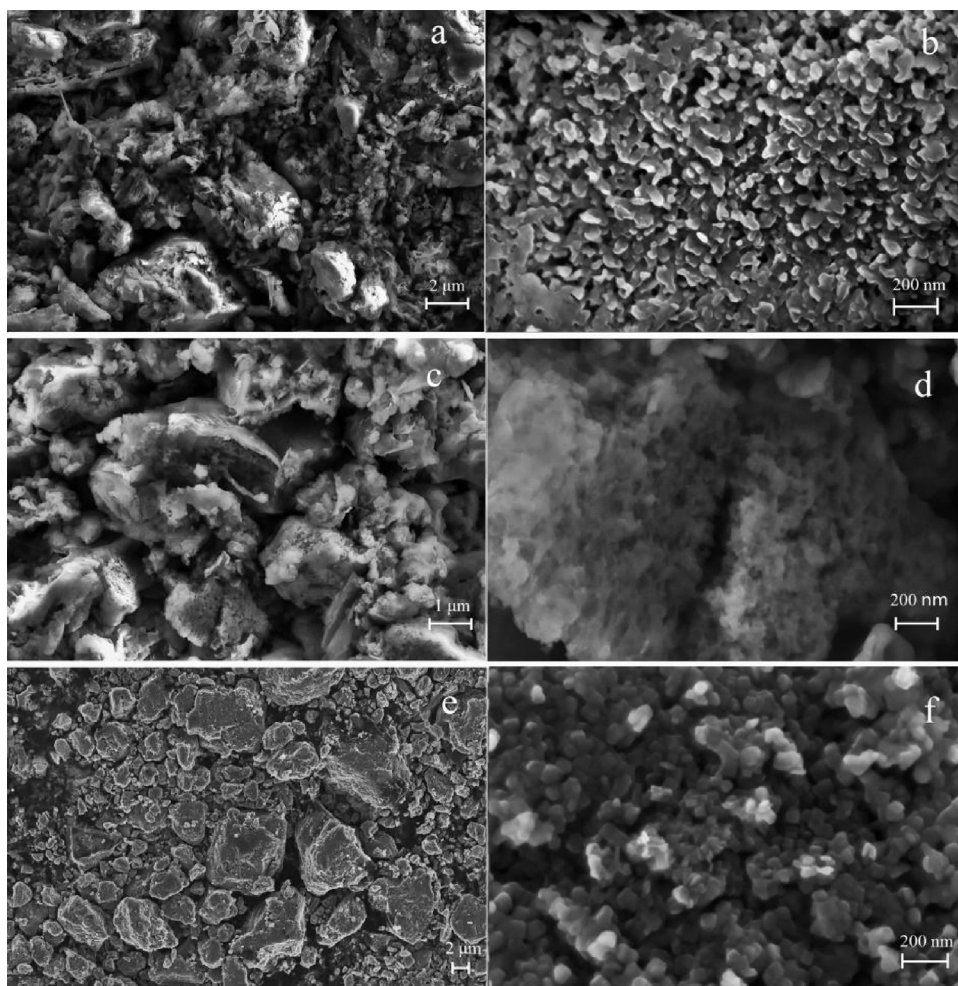**Fig. 7.** Nitrogen adsorption-desorption isotherms of RuC@g-$C_3N_4$ (a) and RuC@g-$C_3N_4$/$TiO_2$ hybrid (G12-1) (b).

**Fig. 8.** FE-SEM images of g-C$_3$N$_4$ (a) (b), RuC@g-C$_3$N$_4$ (c) (d), RuC@g-C$_3$N$_4$/TiO$_2$ hybrid (G12-1) (e) (f).

The peaks at 478 nm are attributed to the ruthenium complexes, and all the samples exhibit strong visible light absorption with absorption edges at around 370–450 nm. As shown in Fig. 12, the absorption edges of RuC@g-C$_3$N$_4$/TiO$_2$ hybrids are extended to visible light to some extent with increase of g-C$_3$N$_4$. Obviously, the heterojunction between TiO$_2$ and g-C$_3$N$_4$ has no enough capacity to change the band gaps of RuC@g-C$_3$N$_4$/TiO$_2$ and g-C$_3$N$_4$/TiO$_2$ hybrids because the absorption edges of TiO$_2$ and g-C$_3$N$_4$ are 370 nm and 450 nm nearly, respectively. Therefore, the mechanism is different from that introducing minor amount of other elements into the lattice of semiconductor.

### 3.8. Photocatalytic performance

In order to compare the photocatalytic abilities of the various catalysts quantitatively, the different RuC@g-C$_3$N$_4$/TiO$_2$ hybrids (G14-1, G12-1, G6-1 and G4-1), g-C$_3$N$_4$/TiO$_2$ hybrid (H12-1), RuC@g-C$_3$N$_4$, RuC/TiO$_2$, g-C$_3$N$_4$, TiO$_2$, and control sample without photocatalyst induced photocatalytic degradation of MB under visible light as shown in Fig. S6 of Supplementary Material. In Fig.S6, the relative concentrations of MB decreases with photocatalysis except that g-C$_3$N$_4$ and control sample almost do not make degradation of the MB in visible irradiation. The g-C$_3$N$_4$ almost has not effect on degradation of MB due to the high recombination rate of e$^-$-h$^+$ pairs in tris-s-triazine units, whereas the TiO$_2$ shows an efficiency of degradation at ~21% degradation within 3 h of irradiation. The obvious activity TiO$_2$ may be attributed to defected-TiO$_2$ which is much more active than pure TiO$_2$ under both UV and visible light [54]. Further, the pseudo-first-order photodegradation could be described as $ln(C_0/C_t) = kt$, where $C_0$ is the initial concentration of MB, $C_t$ is the rest concentration of MB at the

irradiation time $t$, and $k$ is the kinetic constant. The time-course variation of $ln(C_0/C_t)$ with error bar is exhibited as shown in Fig. 13. As it can be seen, the plots of $ln(C_0/C_t)$ against $t$ are nearly linear, and the corresponding kinetic constants of G12-1, G6-1, G14-1, G4-1, H12-1, RuC@g-C$_3$N$_4$, RuC/TiO$_2$, and TiO$_2$ are shown in Table 3. In addition, the kinetic constants of g-C$_3$N$_4$ and control sample are about 0.0015 min$^{-1}$ and 0.00019 min$^{-1}$, respectively[24]. After the ruthenium complexes sensitizing, the RuC/TiO$_2$, RuC@g-C$_3$N$_4$ and RuC@g-C$_3$N$_4$/TiO$_2$ hybrid (G12-1) perform higher kinetic constants with 0.0038 min$^{-1}$, 0.0066 min$^{-1}$, 0.0336 min$^{-1}$ than TiO$_2$, g-C$_3$N$_4$ and g-C$_3$N$_4$/TiO$_2$ hybrid (H12-1) with 0.0018 min$^{-1}$, 0.0015 min$^{-1}$, 0.0176 min$^{-1}$ respectively as shown in Table 3. The result suggests that the ruthenium complexes sensitizing can usefully improve the photocatalytic performance [55,56], and the optimal theory mass ratio of TiO$_2$/RuC@g-C$_3$N$_4$ of 12:1 presents the best catalytic performance, and it is nearly 1.9 times as high as the conventional reported optimal g-C$_3$N$_4$/TiO$_2$ hybrid (H12-1) under visible light irradiation.

### 3.9. Mechanism

The proposal mechanism for photogenerated electron-hole separation and transport in the RuC@g-C$_3$N$_4$/TiO$_2$ hybrid under visible-light irradiation is illustrated in Fig. 14. Several reactive species would generate for RuC@g-C$_3$N$_4$/TiO$_2$ hybrid through the reactions with the holes and electrons, which are considered to be involved in the actual oxidative and reductive reactions. The species are generally called reactive oxygen species including superoxide anion radical ($\cdot$O$_2{}^-$), hydrogen peroxide (H$_2$O$_2$), singlet oxygen ($^1$O$_2$), and hydroxyl radical ($\cdot$OH) [57], which have enough strong reactivity to degrade almost all
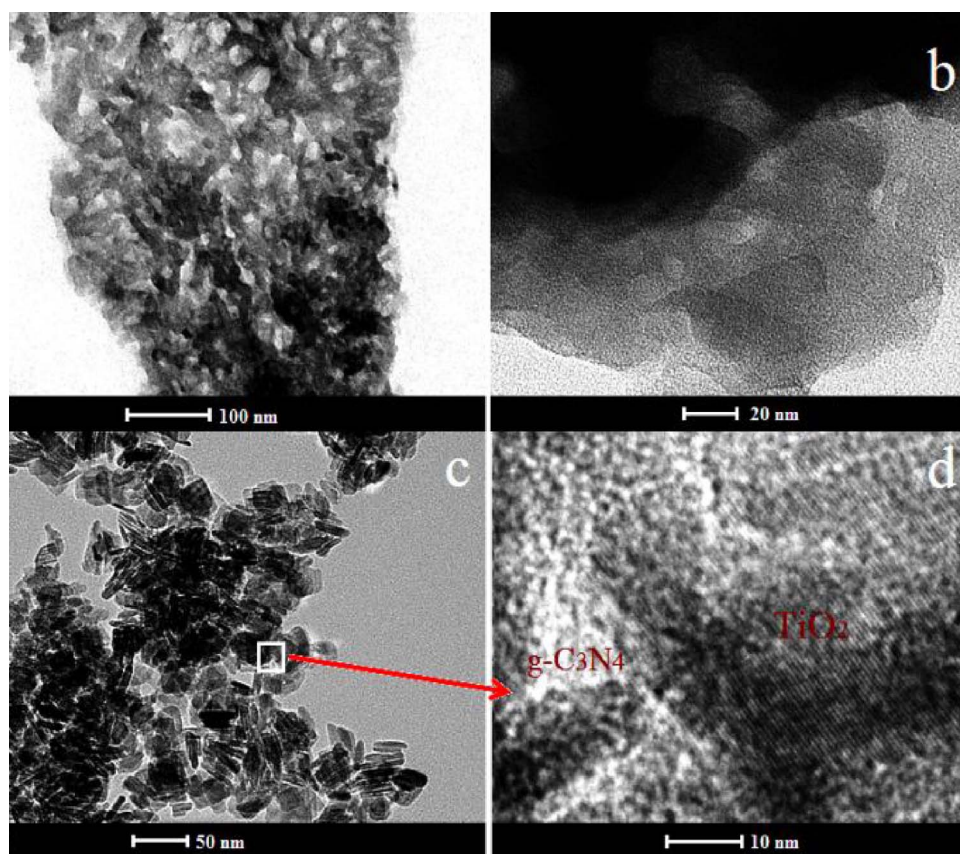
organic pollution. The conduction band (CB) and valence band (VB) edge potentials of are at −1.11 eV and 1.56 eV for g-C$_3$N$_4$, and are at −0.23 eV and 2.85 eV for TiO$_2$, respectively. For g-C$_3$N$_4$/TiO$_2$ hybrid (H12-1), g-C$_3$N$_4$ would absorb visible light and be easily excited to provide the holes and electrons, and the photoinduced electrons converged on the surface of g-C$_3$N$_4$ are easily transferred to TiO$_2$ because of the CB edge potential of g-C$_3$N$_4$ is more negative than that of TiO$_2$, then the electrons accumulated in the CB of TiO$_2$ can be transferred and dissolved in oxygen to form ·O$_2^-$, which then reacts to finally produce active ·OH radicals as follows [57]:
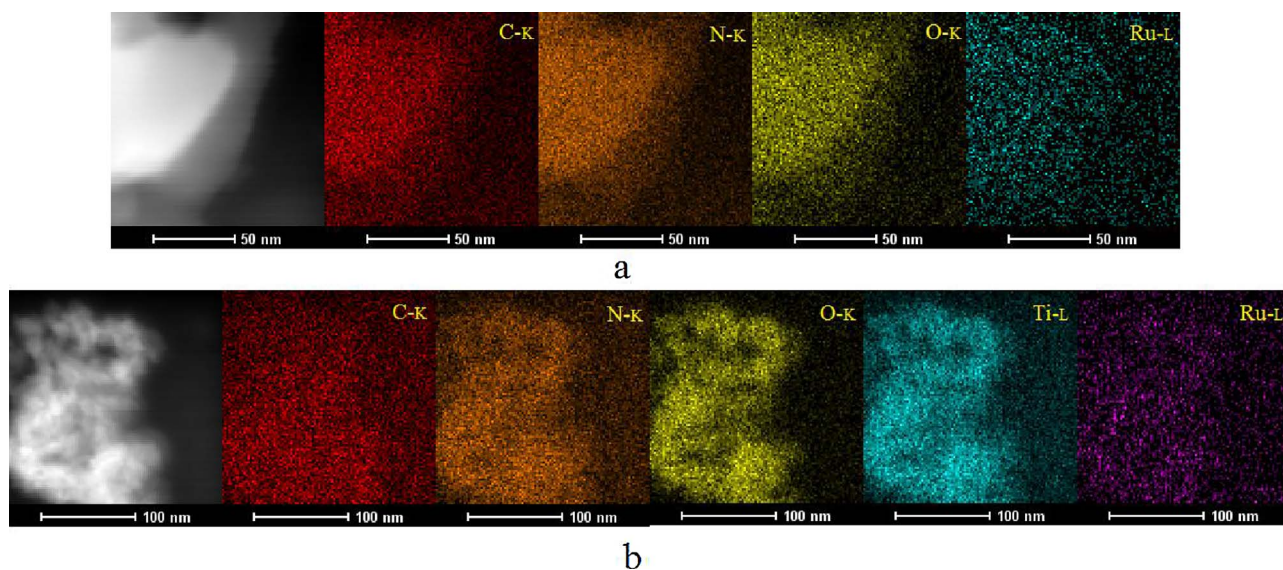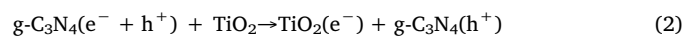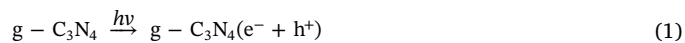
$$g - C_3N_4 \xrightarrow{h\nu} g - C_3N_4(e^- + h^+) \tag{1}$$

$$g\text{-}C_3N_4(e^- + h^+) + TiO_2 \rightarrow TiO_2(e^-) + g\text{-}C_3N_4(h^+) \tag{2}$$

$$TiO_2(e^-) + O_2 \rightarrow \cdot O_2^- \tag{3}$$

$$\cdot O_2^- + H^+ \rightarrow \cdot HO_2 \tag{4}$$

$$TiO_2(e^-) + \cdot HO_2 \rightarrow HO_2^- \tag{5}$$

$$HO_2^- + H^+ \rightarrow H_2O_2 \tag{6}$$



**Fig. 10.** Element mapping of RuC@g-C$_3$N$_4$ (a) and RuC@g-C$_3$N$_4$/TiO$_2$ hybrid (G12-1) (b) by HRTEM.
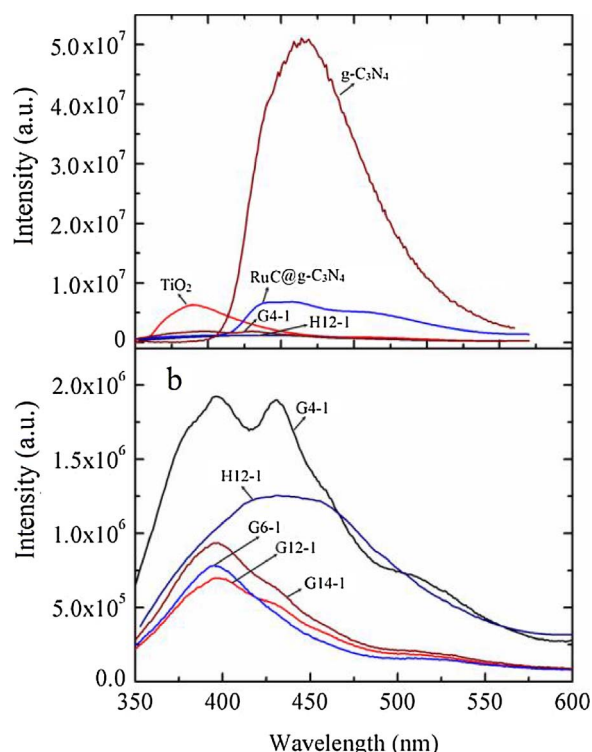
**Fig. 11.** PL spectra of different RuC@g-C$_3$N$_4$/TiO$_2$ hybrids (G14-1, G12-1, G6-1 and G4-1), g-C$_3$N$_4$, TiO$_2$ and g-C$_3$N$_4$/TiO$_2$ hybrid (H12-1).
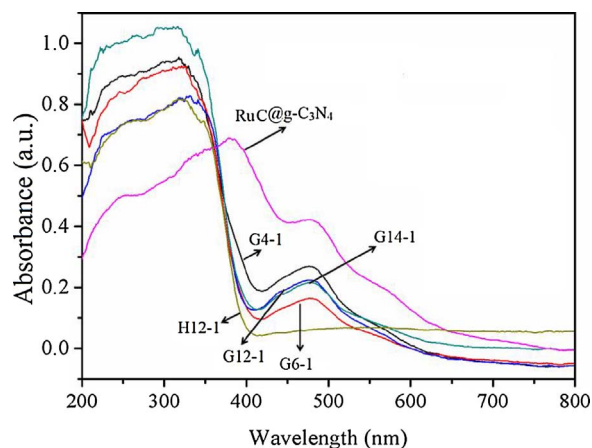


**Fig. 12.** UV–vis DRS spectra of different RuC@g-C$_3$N$_4$/TiO$_2$ hybrids (G14-1, G12-1, G6-1 and G4-1) and g-C$_3$N$_4$/TiO$_2$ hybrid (H12-1).

$$TiO_2(e^-) + H_2O_2 \rightarrow \cdot OH + OH^- \tag{7}$$

Because the VB potential of g-C$_3$N$_4$ is more negative than $E_0$ ($\cdot$HO/OH$^-$ = + 1.99 eV), the holes in the VB of g-C$_3$N$_4$ cannot oxidize OH$^-$ or H$_2$O to form $\cdot$HO, however the holes are also likely to participate in the photocatalytic degradation reaction. As a result, by the generated $\cdot$O$_2^-$, $\cdot$HO and hole, the MB molecules produce CO$_2$ and H$_2$O as final products. The process is described as follows:

$$\cdot HO + \cdot O_2^-, h^+ + MB \rightarrow \text{Degradation product} \tag{8}$$
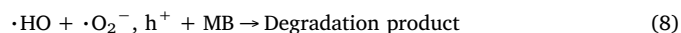
Ruthenium complexes have the strong light absorption and high quantum efficiency, and it will produce the RuC$^{2+*}$ molecule in the excited state. The ruthenium complexes and g-C$_3$N$_4$ are immobilized together through the chemical bond, so the excited state of the RuC$^{2+*}$ molecule is easy to transfer electrons to the CB of g-C$_3$N$_4$, and it's not easily recombined with RuC$^{2+}$. This process can be described by the
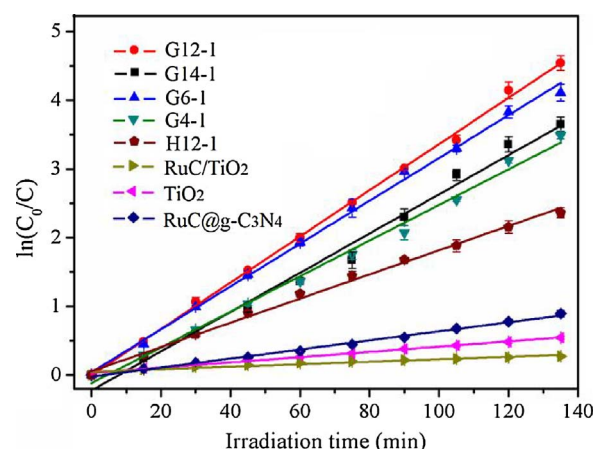


**Fig. 13.** Linear transform $ln(C_0/C)$ of the kinetic curves of photocatalytic degradation of MB using different RuC@g-C$_3$N$_4$/TiO$_2$ hybrids (G14-1, G12-1, G6-1 and G4-1), g-C$_3$N$_4$/TiO$_2$ hybrid (H12-1), RuC@g-C$_3$N$_4$, RuC/TiO$_2$, and TiO$_2$ under visible light irradiation.

**Table 3**
Kinetic constant of different photocatalysts.

| Photocatalyst | Kinetic constant ($k$)/min$^{-1}$ |
|---|---|
| G14-1 | 0.0286 |
| G12-1 | 0.0336 |
| G6-1 | 0.0312 |
| G4-1 | 0.0260 |
| H12-1 | 0.0176 |
| RuC@g-C$_3$N$_4$ | 0.0066 |
| RuC/TiO$_2$ | 0.0038 |
| TiO$_2$ | 0.0018 |
| g-C$_3$N$_4$ | 0.0015 |
| Control sample | 0.00019 |

following two formulas [25]:

$$RUC^{2+} \overset{h\nu}{\rightarrow} RUC^{2+*} \tag{9}$$

$$RuC^{2+*} + g\text{-}C_3N_4 \rightarrow RuC^{2+} + g\text{-}C_3N_4(e^-) \tag{10}$$
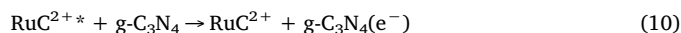
Obviously, the ruthenium complexes could even more improve the efficiency of charge separation and photocatalytic performance.

## 4. Conclusions

The square flake-like TiO$_2$ crystal with the side length 50–60 nm and the thickness of 10–15 nm was deposited on the surface of RuC@g-C$_3$N$_4$ through solvothermal method, which formed the interface of hetero-structure between g-C$_3$N$_4$ and TiO$_2$, and minor Ru element was equidistributed on the surface of RuC@g-C$_3$N$_4$/TiO$_2$ powder. The optimal RuC@g-C$_3$N$_4$/TiO$_2$ hybrid with the mass ratio of TiO$_2$ to RuC@g-C$_3$N$_4$ of 12:1 as well as RuC about 0.44 wt.% of G12-1 performed the best photocatalytic kinetic constant of 0.0336 min$^{-1}$, which was nearly 1.91 times as high as that of the conventional g-C$_3$N$_4$/TiO$_2$ hybrid (H12-1) under the visible light irradiation. The heterojunction in RuC@g-C$_3$N$_4$/TiO$_2$ hybrid could promote the separation efficiency of the photogenerated electrons and holes (e$^-$/h$^+$). Further research results indicated that the minor ruthenium complexes as a photosensitizer introduced to g-C$_3$N$_4$ not only could effectively separate photogenerated electron-hole pairs, but also usefully increase the quantity of photon absorption and then transfer electrons from the excited state of the ruthenium complexes molecule to the conduction band of g-C$_3$N$_4$, as a result, more improve the quantum efficiency of the g-C$_3$N$_4$/TiO$_2$ hybrid. The minor ruthenium complexes sensitizing g-C$_3$N$_4$/TiO$_2$ hybrid would like to be expected to have promising applications in photocatalysis and
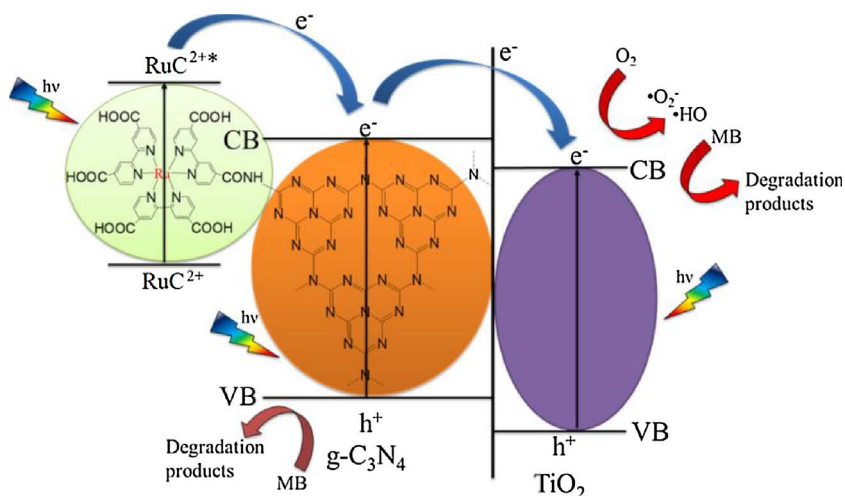
Fig. 14. Proposal mechanism for the photoexcited electron-hole separation and transport processes in RuC@g-$C_3N_4$/$TiO_2$ hybrid.

many other solar light application fields.

## Appendix A. Supplementary data

Supplementary data associated with this article can be found, in the online version, at https://doi.org/10.1016/j.apcatb.2018.01.034.

## References

[1] L. Chu, J. Wang, J. Dong, H. Liu, X. Sun, Chemosphere 86 (2012) 409.
[2] W.D. Wilson, C.M. Schaldach, W.L. Bourcier, P.H. Paul, US patent. US 7,632, 406 B2.
[3] M.A. Martin-Lara, G. Blazquez, M.C. Trujillo, A. Perez, M. Calero, J. Clean. Prod. 81 (2014) 120–129.
[4] Y. Zhang, B. Hui, L. Ye, RSC Adv. 5 (2015) 91414–91422.
[5] O. Gimeno, J.F. García-Araya, F.J. Beltrán, F.J. Rivas, A. Espejo, Chem. Eng. J. 290 (2016) 12–20.
[6] A. Fujishima, K. Honda, Nature 238 (1972) 37–38.
[7] R.P. Cavalcante, R.F. Dantas, H. Wender, B. Bayarri, O. González, J. Giménez, S. Esplugas, A. Machulek, Appl. Catal. B Environ. 176–177 (2015) 173–182.
[8] J. Lu, Y. Wang, J. Huang, J. Fei, L. Cao, C. Li, Dyes Pigm. 144 (2017) 203–211.
[9] J.T. Park, D.J. Kim, D.H. Kim, J.H. Kim, Mater. Lett. 202 (2017) 66–69.
[10] C. McManamon, J. O'Connell, P. Delaney, S. Rasappa, J.D. Holmes, M.A. Morris, J. Mol. Catal. A Chem. 406 (2015) 51–57.
[11] S.P. Madhusudanan, B. Gangaja, A.G. Shyla, A.S. Nair, S.V. Nair, D. Santhanagopalan, ACS Sustain. Chem. Eng. 5 (2017) 2393–2399.
[12] T. Wang, D. Shen, T. Xu, R. Jiang, Sci. Total Environ. 586 (2017) 347–354.
[13] Q. Wang, R. Jin, M. Zhang, S. Gao, J. Alloy. Compd. 690 (2017) 139–144.
[14] M. Asemi, S. Maleki, M. Ghanaatshoar, J. Sol-Gel Sci. Technol. 81 (2017) 645–651.
[15] H. Su, Y. Huang, Y. Chang, P. Zhai, N.Y. Hau, P.C.H. Cheung, W. Yeh, T. Wei, S. Feng, Electrochim. Acta 182 (2015) 230–237.
[16] Z. Chen, Y. Li, M. Guo, F. Xu, P. Wang, Y. Du, P. Na, J. Hazard. Mater. 310 (2016) 188–198.
[17] J. Wang, Z. Guang, J. Huang, Q. Li, J. Yang, J. Mater. Chem. A 2 (2014) 7960–7966.
[18] M.Q. Wen, T. Xiong, Z.G. Zang, W. Wei, X.T. Tang, F. Dong, Opt. Express 10 (2016) 10205–10212.
[19] L. Zhang, F. Huang, L. Zhou, J. Mater. Sci. 50 (2015) 3057–3064.
[20] Y. Shi, S. Jiang, K. Zhou, B. Wang, B. Wang, Z. Gui, Y. Hu, R.K.K. Yuen, RSC Adv. 4 (2014) 2609.
[21] L. Liu, G. Zhang, J.T.S. Irvine, Y. Wu, Energy Technol. 3 (2015) 982–988.
[22] X. Chen, J. Wei, R. Hou, Y. Liang, Z. Xie, Y. Zhu, X. Zhang, H. Wang, Appl. Catal. B Environ. 188 (2016) 342–350.
[23] G. Jiang, X. Yang, Y. Wu, Z. Li, Y. Han, X. Shen, J. Mol. Catal. A 432 (2017) 232–241.
[24] Z. Li, G. Jiang, Z. Zhang, Y. Wu, Y. Han, J. Mol. Catal. A Chem. 425 (2016) 340–348.
[25] T.J. Meyer, R.C. Young, D.G. Whitten, J. Am. Chem. Soc. (1975) 4781–4782.
[26] D. Kuang, S. Ito, B. Wenger, C. Klein, J. Moser, R. Humphry-Baker, S.M. Zakeeruddin, M. Grätzel, J. Am. Chem. Soc. 128 (2006) 4146–4154.
[27] Y. Ooyama, S. Inoue, T. Nagano, K. Kushimoto, J. Ohshita, I. Imae, K. Komaguchi, Y. Harima, Angew. Chem. Int. Ed. 50 (2011) 7429–7433.
[28] D. Kuang, S. Uchida, R. Humphry-Baker, S.M. Zakeeruddin, M. Grätzel, Angew. Chem. Int. Ed. 47 (2008) 1923–1927.
[29] T. Ooyama, S. Nagano, I. Inoue, K. Imae, J. Komaguchi, Y. Ohshita, Chem. A Eur. J. 17 (2011) 14837–14843.
[30] M.K. Nazeeruddin, A. Kay, I. Rodicio, R. Humphrybaker, E. Muller, P. Liska, N. Vlachopoulos, M. Grätzel, J. Am. Chem. Soc. 115 (1993) 6382–6390.
[31] K. Maeda, K. Sekizawa, O. Ishitani, Chem. Commun. 49 (2013) 10127–10129.
[32] E. Kowalska, K. Yoshiiri, Z. Wei, S. Zheng, E. Kastl, H. Remita, B. Ohtani, S. Rau, Appl. Catal. B Environ. 178 (2015) 133–143.
[33] E. Eskelinen, S. Luukkanen, M. Haukka, M. Ahlgrén, T.A. Pakkanen, J. Chem. Soc. Dalton Trans. (2000) 2745–2752.
[34] S. Grammenudi, M. Franke, F. Vögtle, E. Steckhan, J. Ind. Microbiol. 5 (1987) 695–707.
[35] W. Lu, T. Xu, Y. Wang, H. Hu, N. Li, X. Jiang, Appl. Catal. B Environ. 180 (2016) 20–28.
[36] X. Wang, K. Maeda, A. Thomas, K. Takanabe, G. Xin, J.M. Carlsson, K. Domen, M. Antonietti, Nat. Mater. 8 (2009) 76–80.
[37] P. Niu, L. Zhang, G. Liu, H. Cheng, Adv. Funct. Mater. 22 (2012) 4763–4770.
[38] S. Ngamta, N. Boonprakob, N. Wetchakun, K. Ounnunkad, S. Phanichphant, B. Inceesungvorn, Mater. Lett. 105 (2013) 76–79.
[39] Q. Li, Y. He, R. Peng, Rsc. Adv. 5 (2015) 24507–24512.
[40] S.C. Yan, Z.S. Li, Z.G. Zou, Langmuir 25 (2009) 10397–10401.
[41] Y. Qiu, L. Gao, Chem. Commun. (2003) 2378–2379.
[42] X. Song, Y. Hu, M. Zheng, C. Wei, Appl. Catal. B Environ. 182 (2016) 587–597.
[43] Y. Du, H.X. Fang, Q. Zhang, H.L. Zhang, Z. Hong, Spectrochim. Acta A Mol. Biomol. Spectrosc. 153 (2016) 580–585.
[44] C. Miranda, H. Mansilla, S. Yáñez, S. Obregón, G. Colón, J. Photochem. Photobiol. A Chem. 253 (2013) 16–21.
[45] L. Liu, D. Ma, H. Zheng, X. Li, M. Cheng, X. Bao, Microporous Mesoporous Mater. 110 (2008) 216–222.
[46] N. Boonprakob, N. Wetchakun, S. Phanichphant, D. Waxler, P. Sherrell, A. Nattestad, J. Chen, B. Inceesungvorn, J. Colloid Interfaces Sci. 417 (2014) 402–409.
[47] D.J. Martin, K. Qiu, S.A. Shevlin, A.D. Handoko, X. Chen, Z. Guo, J. Tang, Angew. Chem. Int. Ed. 53 (2014) 9240–9245.
[48] J. Li, B. Shen, Z. Hong, B. Lin, B. Gao, Y. Chen, Chem. Commun. 48 (2012) 12017.
[49] S. Sayan, S. Suzer, D.O. Uner, J. Mol. Struct. 410 (1997) 111–114.
[50] X. Lin, K. Yang, R. Si, X. Chen, W. Dai, X. Fu, Appl. Catal. B Environ. 147 (2014) 585–591.
[51] Z. Huang, J. Song, L. Pan, Z. Wang, X. Zhang, J. Zou, W. Mi, X. Zhang, L. Wang, Nano Energy 12 (2015) 646–656.
[52] N. Boonprakob, N. Wetchakun, S. Phanichphant, D. Waxler, P. Sherrell, A. Nattestad, J. Chen, B. Inceesungvorn, J. Colloid Interfaces Sci. 417 (2014) 402–409.
[53] M.K. Nazeeruddin, S.M. Zakeeruddin, R. Humphry-Baker, M. Jirousek, P. Liska, N. Vlachopoulos, V. Shklover, C. Fischer, M. Grätzel, Inorg. Chem. 38 (1999) 6298–6305.
[54] S. Wang, L. Pan, J.J. Song, W. Mi, J.J. Zou, L. Wang, J. Am. Chem. Soc. 137 (2015) 2975–2983.
[55] A. Reynal, E. Palomares, Eur. J. Inorg. Chem. 2011 (2011) 4509–4526.
[56] H. Li, J. Wu, Y.A. Jeilani, C.W. Ingram, I.I. Harruna, J. Nanopart. Res. 14 (2012) 1–14.
[57] Y. Noska, A.Y. Nosaka, Chem. Rev. 117 (2017) 11302–11336.